Vacuum 195 (2022) 110687

Contents lists available at ScienceDirect

Vacuum

journal homepage: www.elsevier.com/locate/vacuum

Preparation and properties of graphene reinforced Cu/0.5$CeO_2$30Cr electrical contact materials

Shuang Liu [a,b,c,1], Lihua Li [a,b,c,*,1], Meng Zhou [a,b,c,**,1], Shengli Liang [a,b,c,1], Yi Zhang [a,b,c,***], Jinliang Huang [a,b,c,****], Baohong Tian [a,b,c], Yongfeng Geng [a,b,c], Yong Liu [a,b,c], Yanlin Jia [d], Xu Li [e], Alex A. Volinsky [f]

[a] School of Materials Science and Engineering, Henan University of Science and Technology, Luoyang, 471023, China
[b] Provincial and Ministerial Co-construction of Collaborative Innovation Center for Non-ferrous Metal New Materials and Advanced Processing Technology, Luoyang, 471023, China
[c] Henan Key Laboratory of Nonferrous Materials Science and Processing Technology, Luoyang, 471023, China
[d] School of Materials Science and Engineering, Central South University, Changsha, 410083, China
[e] Center for Advanced Measurement Science, National Institute of Metrology, Beijing, 100029, China
[f] Department of Mechanical Engineering, University of South Florida, 4202 E. Fowler Ave. ENG030, Tampa, 33620, USA

ARTICLE INFO

Keywords:
Copper matrix composites
Graphene oxide
Ceria nanoparticles
In-situ formation
Electrical contact

ABSTRACT

A graphene reinforced Cu/CeO_2Cr electrical contact material with high strength and electrical conductivity was designed. Graphene oxide (GO) was prepared with modified Hummers' method. Composite powders of GO, ceria nanoparticles, copper and chromium were prepared by freeze-drying. The GO-Cu/0.5$CeO_2$30Cr electrical contact material was prepared by spark plasma sintering. Raman and X-ray photoelectron spectroscopy (XPS) characterization results indicated that during the sintering process, the graphene oxide was transformed into reduced graphene oxide (RGO). In addition, SEM and TEM characterization results indicated that the CeO_2 nanoparticles were uniformly dispersed in the matrix, which hindered the movement of dislocations and improved the strength of the matrix, and a small amount of carbon atoms combined with Cr to form Cr_3C_2, enhancing the interface bonding. Compared with Cu/0.5$CeO_2$30Cr composites, the electrical conductivity, hardness, tensile strength, and welding resistance of the two composites containing 0.5 wt% and 1.0 wt% GO were both improved and the 0.5GO-Cu/0.5$CeO_2$30Cr composites have better welding resistance.

1. Introduction

As shown in Fig. 1, the copper alloys and copper matrix composites are widely used in aerospace and electronics industry due to their high conductivity [1], high thermal conductivity [2], wear resistance [3,4], arc erosion resistance [5] and high temperature stability [6]. With the development of many national projects and the upgrading of power system, the demand for safety and efficiency of related materials is increasing. High voltage circuit breaker is the main electrical control equipment in substation. It cannot only cut off or close the no-load current and load current in high-voltage circuit when the system is in normal operation, but also cooperate with relay protection to cut off the fault current quickly and prevent the expansion of accident scope when the system fails [7,8]. Contact is an indispensable part of high voltage circuit breaker, which is mainly used to connect and disconnect the circuit. In the process of generation, maintenance and elimination of electrical contact, a variety of physical and chemical phenomena will occur [9]. The contact of high-voltage circuit breaker should not have too high temperature rise when passing the current, and it can withstand the destructive effect of intermittent arc [10], thus, the material should have the characteristics of high conductivity and thermal conductivity, wear resistance, arc erosion resistance, anti-welding, and low contact

* Corresponding author. School of Materials Science and Engineering, Henan University of Science and Technology, Luoyang, 471023, China.
** Corresponding author. School of Materials Science and Engineering, Henan University of Science and Technology, Luoyang, 471023, China.
*** Corresponding author. School of Materials Science and Engineering, Henan University of Science and Technology, Luoyang, 471023, China.
**** Corresponding author. School of Materials Science and Engineering, Henan University of Science and Technology, Luoyang, 471023, China.
E-mail addresses: lilihua7818@163.com (L. Li), zhoumeng0902@126.com (M. Zhou), yizhang@huast.edu.cn (Y. Zhang), huangjl@haust.edu.cn (J. Huang).
[1] These authors contributed equally to this work.

https://doi.org/10.1016/j.vacuum.2021.110687
Received 15 June 2021; Received in revised form 12 October 2021; Accepted 13 October 2021
Available online 16 October 2021

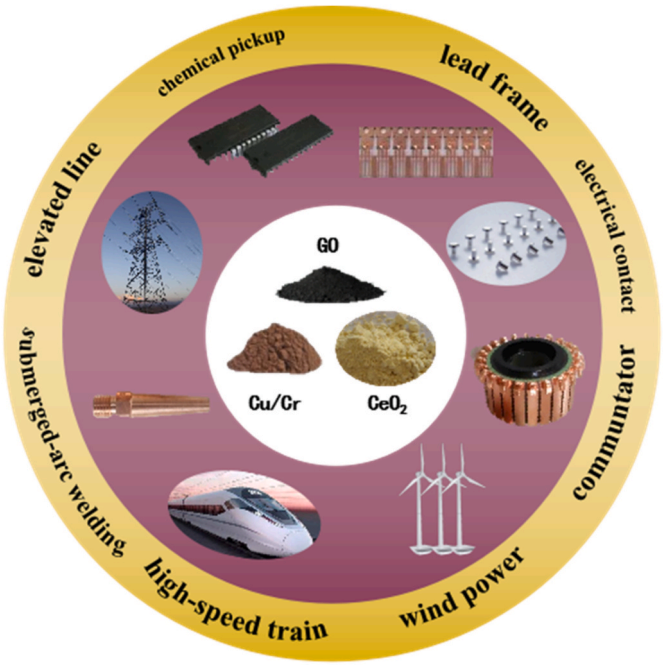

Fig. 1. Application of copper matrix.

resistance. Copper matrix composites can be used as electrical contact materials because of their excellent properties, and different reinforcing phases have different reinforcing effects in the materials [11].

Copper has low melting point, high electrical conductivity, and good plasticity, while chromium has high melting point, mechanical strength, low cut-off value, strong breaking ability, and great affinity for oxygen. Moreover, the low solubility of chromium in copper makes the composite material composed of copper and chromium has the advantages of both phases. Therefore, copper chromium contact is considered as an ideal electrical contact material in high-power field [12]. Due to its special atomic structure and activity, rare earth elements are used as trace additives in metal materials, which can eliminate impurities, refine grains, inhibit recrystallization, and improve material composition [13]. CeO_2 with nanometer size can not only retains the unique electronic layer structure of rare earth elements, but also has the size effect, which makes the material have a high-density interface [14]. Due to the improvement of redox performance, transport performance and specific surface area [15], nanostructured ceria has attracted extensive attention in academic circles, mainly including the design, synthesis, and application of nanostructured ceria [16–20].

Graphene is a new kind of material, which is closely packed with carbon atoms connected by sp^2 hybrid to form a single-layer two-dimensional honeycomb lattice structure [21–23]. It is the two-dimensional crystal material with the highest strength and hardness among the known two-dimensional materials. Its theoretical elastic modulus is as high as 1 TPa, tensile strength reaches 130 GPa, and the thermal conductivity of single-layer graphene as high as 5000 W/mK, which is more than ten times that of copper, in terms of electrical properties. Besides, its carrier mobility can reach 200,000 $cm^2/(V{\cdot}s)$ [24]. Compared with copper, graphene is an ideal reinforcement for the development of high performance, especially high conductivity metal matrix composites [25–30]. Therefore, graphene and its derivatives, such as GO and RGO, have attracted more and more attention as ideal reinforcements of metal matrix composites. Copper matrix composites reinforced with graphene and nano particles not only have high hardness and high strength, but also have high wear resistance and good chemical stability, which is a kind of functional materials with excellent comprehensive properties. Xiaohui Zhang et al. [9] prepared GO/Al_2O_3–Cu/35W5Cr composites by wet grinding and vacuum hot-pressing sintering. The Cr_3C_2 formed in situ possessed high hardness and good wettability to copper, and the interface bonding, interface strength and mechanical properties were enhanced through coupling effect. The tensile strength of the samples with GO were obviously higher than that of the original sample. Ke Chu et al. [31,32] prepared graphene/copper matrix composites by ball milling and hot-pressing sintering. Compared with pure copper, the yield strength and Young's modulus of the composites with 8 vol% GNP increased by 114% and 37%, respectively. In addition, a small amount of Cr_7C_3 layer/nanoparticles were formed on the RGO/CuCr interface, which greatly improved the interface bonding of the composites. The tensile strength of 2.5 vol% RGO/CuCr composite was 352 MPa, 82% and 19% higher than CuCr alloy and 2.5 vol% RGO/Cu composite, respectively. The increase of strength of RGO/CuCr composites was attributed to the dual role of Cr_7C_3 layer/nanoparticles, which not only improved the load transfer efficiency, but also improved the dislocation strengthening ability of RGO itself. Yakun Chen et al. [33] prepared graphene/copper composites by in-situ growth method and vacuum sintering. The strengthening effect of in-situ grown graphene in the matrix promoted load transfer and dislocation strengthening. The yield strength and tensile strength of the sample containing 0.95 wt% graphene were 244 MPa and 274 MPa, respectively, 17.7% and 27.4% higher than pure Cu. Based on the strategy of powder metallurgy, a three-dimensional continuous graphene network structure was constructed by Xiang Zhang et al. [34] in copper matrix with thermal stress-induced welding between graphene like nanosheets grown on the surface of copper powder. The interpenetrating structural characteristics of the composites not only increased the interfacial shear stress to a higher level, but also significantly enhanced the load transfer strengthening and crack bridging toughening. At the same time, the conductivity and thermal conductivity of additional three-dimensional Super channels were also constructed. Many studies [35–44] have shown that the mechanical properties of metal matrix composites doped with graphene nanocrystals, graphene oxide or reduced graphene oxide have been improved to a certain extent.

We proposed to investigate the strengthening effect of graphene and nanoparticles in metal matrix by the improving Hummers' method and spark plasma sintering (SPS) process. This method avoids the agglomeration and thermal damage of graphene sheets in the preparation process of graphene/metal nanocomposites. The first key point was the uniform dispersion of graphene. Ultrasonic dispersion and freeze-drying were used to avoid the agglomeration of graphene, so that graphene can be dispersed evenly and form chemical bonding with nanoparticles and composite matrix. The second key point was SPS, which solidified the metal powders by local Joule heating and spark plasma generated between individual powders [45,46]. The self-heating generated by the discharge between the powder particles accelerated the heating and cooling rate, which not only limited the growth and diffusion of the grains in the sintering process, but also reduced the average sintering temperature [47,48].

2. Materials and methods

2.1. Experimental materials

Cu powder with an average particle size of 5–10 μm (purity≥99.95%) were provided by Nangong Xiangfan alloy material Co., Ltd.; Cr powder with an average particle size of 44 μm (purity≥99.95%) was provided by Beijing Xing Rong Yuan Technology Co., Ltd.; ceria powder with an average particle size of 50 nm (purity≥99.95%) was provided by Shanghai Aladdin Biochemical Technology Co., Ltd. Graphite powder (purity≥99.5%, 300 mesh), concentrated sulfuric acid (the drug content is 95% and 98%), sodium nitrate (content≥99%) and potassium permanganate (content≥99.5%) were weighed in the ratio of 1 g: 30 ml: 0.5 g: 6 g.

2.2. GO-Cu/0.5CeO_2/30Cr preparation of electrical contact materials

Add concentrated sulfuric acid, sodium nitrate and graphite powder into the beaker in turn, continuously stir in the ice water bath, keep the system temperature below 5 °C, then add potassium permanganate in three times, with an interval of 10 min each time, keep the system temperature below 20 °C, react for 2 h, raise the temperature to 35 °C, continue to react, continue to raise the temperature to 90 °C, and add deionized water react for 30 min 30% hydrogen peroxide was added and stirred in a water bath at 33 °C, then centrifuged washed with dilute hydrochloric acid and deionized water, and freeze-dried (LGJ-12 freeze dryer) for standby. A certain amount of graphene oxide and cerium oxide were dissolved in deionized water and ultrasonically dispersed (KQ-100 Ultrasonic Cleaners) to prepare suspension. The ball milled Cu and Cr composite powder for 4 h at 350 rpm (QM-3SP2 planetary ball mill) was added and mechanically stirred (JJ-1) at 300 rpm for 30 min, the composite powder was obtained after freeze-drying. Graphene and nano particles reinforced copper chromium electrical contact materials were prepared by densification in spark plasma sintering furnace (SPS-20T-10). Process parameters of spark plasma sintering: sintering temperature 900 °C, pressure 30 MPa, holding time 10 min. The experimental process is shown in Fig. 2.

2.3. Performance test

The conductivity of the sample is measured by conductivity meter (Sigma 2008B1). The relative density of samples was measured and calculated by Archimedes method (MS304S density instrument). The hardness was measured by Vickers hardness tester (HV-100). The tensile test was carried out by universal testing machine (SHIMADZU AG-I 250 KN) at room temperature. X-ray diffraction (XRD) and Raman spectroscopy were used to analyze the phase. The structure of GO was analyzed by X-ray photoelectron spectroscopy (XPS), the excitation source was Mg Kα-1253.6 eV, the electron emission angle was 0°, the size of analyzed area was 650 μm, the samples were not sputtered, etched, and no charge neutralizer was used before analysis. The base pressure during analyses was 3.5×10^{-7} Pa [49]. However, it is a very uncertain process to adjust the spectrum obtained from the experiment with reference to the C1s peak. As a typical unknown compound, amorphous carbon is not included in the sample. Direct alignment of them will lead to error in the results [50,51]. Therefore, the work function method [52] needs to be used, which will produce less error than adjusting the spectrum only with reference to the traditional C 1s peak. The negative bias voltage can be applied to the sample, and the cut-off edge of the low kinetic energy secondary electron can be obtained by collecting the secondary electron data at the low kinetic energy end, so as to calculate the work function of the material [53,54]. Through UPS experiments and calculations, the work functions of two composite materials 0.5GO-Cu/0.5$CeO_2$30Cr and 1.0GO-Cu/0.5-$CeO_2$30Cr are obtained Φ_{SA} are 4.46 eV and 4.35 eV, respectively, there is a relationship between the samples under experimental conditions $E_B^F + \Phi_{SA} = 289.58$ eV, so the values of E_B^F are 285.12 eV and 285.23 eV, the binding energy of the C 1s peak is denoted as E_B^F [49]. JEM-2100 transmission electron microscope (TEM) and JSM-7800F field emission scanning electron microscope (SEM) were used to analyze the microstructure of the samples. Finally, the electrical contact experiment was carried out with JF04C electrical contact test system.

3. Results and discussion

3.1. Morphology of graphene oxide and composite powder

Fig. 3(a and b) shows the TEM and HRTEM images of GO edge. It can be seen from the figures that there are many folds and overlaps on the boundary of GO. The folds and overlaps between lamellae mean that oxygen-containing functional groups are successfully introduced. Hydroxyl and carboxyl groups are distributed on the edge of GO, which makes the edge of GO curl and fold inward [55]. The Fresnel fringes of GO can be clearly seen from the high-resolution image, and the number of layers of GO is estimated to be less than 10, which indicates that the structure of GO obtained by oxidation of graphite is very good. The composite powders were analyzed by SEM and GO flakes were observed in the scanning images of the two composite powders in Fig. 3(c and d). After ball milling and freeze-drying, the structure of GO sheets in composite powders are intact and favorable. Copper powder, chromium powder and ceria nanoparticles were observed on the surface of the thin sheet with uniform distribution. The element content of GO in the composite powders was determined by EDS point scanning, which are shown in Fig. 3(e and f). Dark field images of GO in 0.5GO-Cu/0.5-$CeO_2$30Cr, 1.0GO-Cu/0.5$CeO_2$30Cr composite powders are shown in Fig. 3(g and h), which is a typical diffraction ring of graphene oxide. In order to further determine the existence of graphene oxide, the composites were characterized by XRD, Raman and XPS, as shown in Fig. 4.

3.2. XRD, Raman and XPS analysis of graphene oxide and composite powders

Fig. 4(a) shows the XRD patterns of graphite and GO. It can be seen

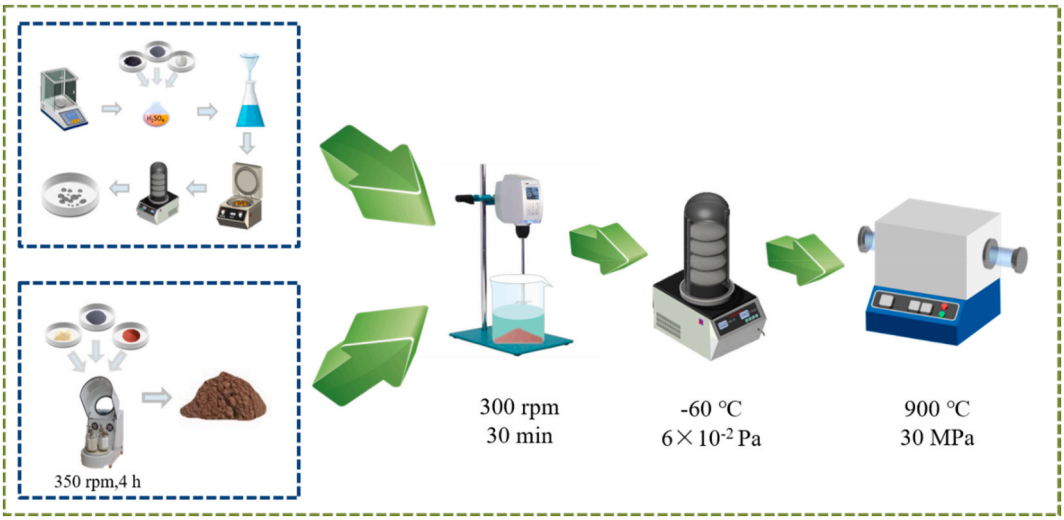

Fig. 2. The experimental process.

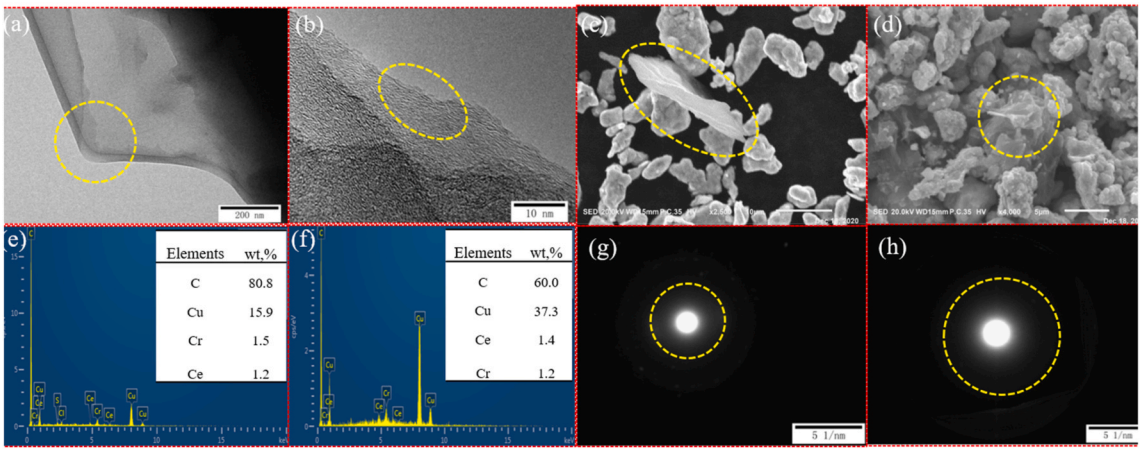

Fig. 3. (a, b) TEM/HRTEM images of GO; (c, d) SEM images of 0.5GO-Cu/0.5$CeO_2$30Cr, 1.0GO-Cu/0.5$CeO_2$30Cr composite powders; (e, f) EDS points scanning of GO in 0.5GO-Cu/0.5$CeO_2$30Cr, 1.0GO-Cu/0.5$CeO_2$30Cr composite powders; (g, h) Dark field images of GO in 0.5GO-Cu/0.5$CeO_2$30Cr, 1.0GO-Cu/0.5$CeO_2$30Cr composite powders.

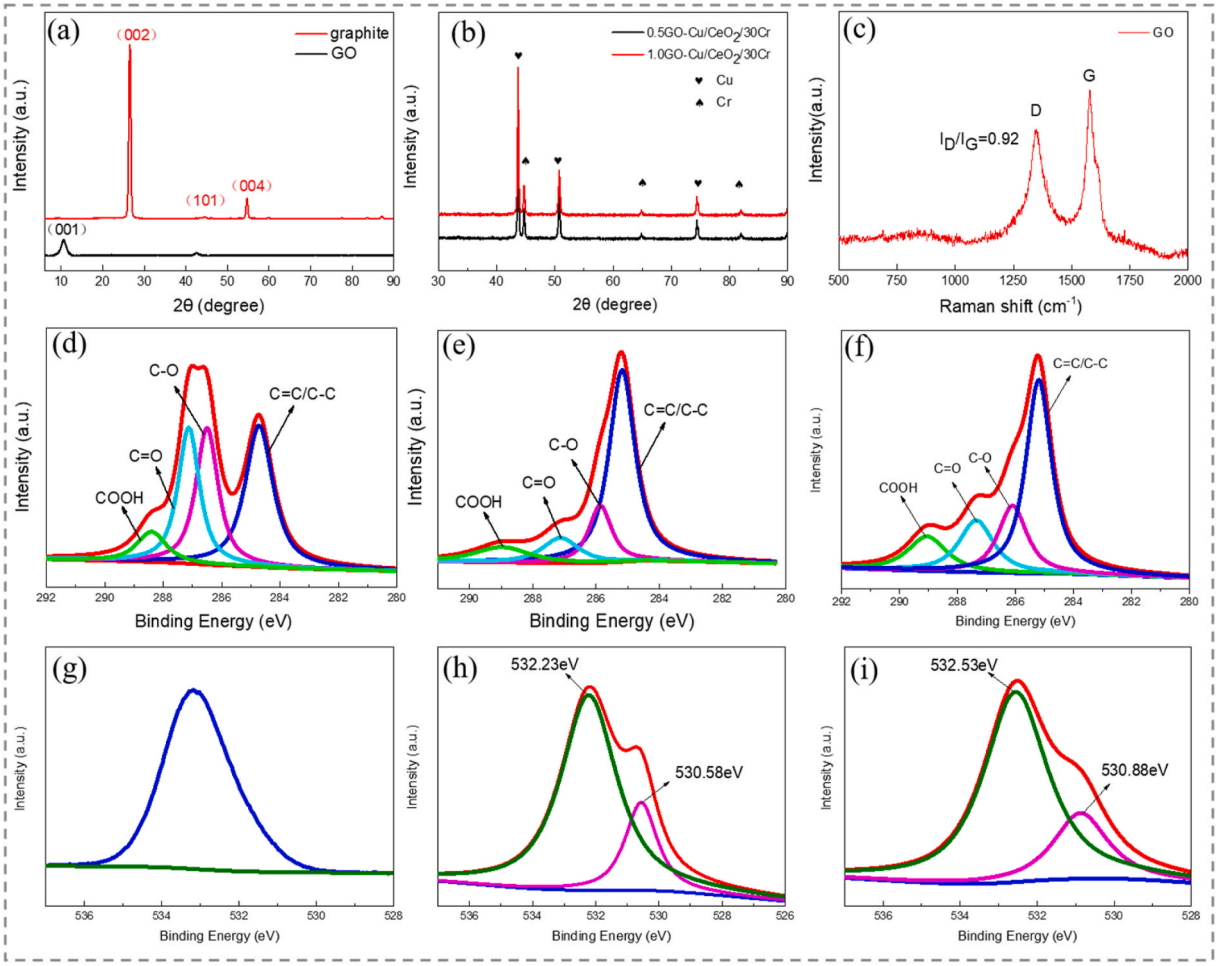

Fig. 4. (a) XRD patterns of graphene oxide and graphite; (b) XRD patterns of composites; (c) Raman spectra of GO; (d) XPS analysis of GO-C 1s; (e) XPS analysis of 0.5GO-Cu/0.5$CeO_2$30Cr –C 1s; (f) XPS analysis of 1.0GO-Cu/0.5$CeO_2$30Cr –C 1s; (g) XPS analysis of GO-O 1s; (h) XPS analysis of 0.5GO-Cu/0.5$CeO_2$30Cr –O 1s; (i) XPS analysis of 1.0GO-Cu/0.5$CeO_2$30Cr –O 1s.

from the figure that there is a high intensity and sharp (002) diffraction peak of graphite at about $2\theta = 26.5°$and the layer spacing d = 0.34 nm can be calculated according to the Bragg equation ($2d\sin\theta = n\lambda$). At the same time, weak diffraction peaks such as (101) (004) appeared. When graphite is oxidized to graphite oxide by concentrated sulfuric acid and potassium permanganate strong oxidant, the characteristic peak of graphite at $2\theta = 26.5°$and the diffraction peaks of other crystal planes disappear, while a (001) characteristic diffraction peak of GO appears at about $2\theta = 10.3°$ and the interlayer spacing increases to d = 0.86 nm, which is nearly three times of the interlayer spacing of graphite.

This is mainly because the intercalation oxidation of oxygen-containing functional groups destroys the intermolecular force between the graphite sheets, and makes the carbon atom layer spacing of graphite increase sharply [56], which indicates that the graphite is completely oxidized. At the same time, the characteristic peak of GO shifts to low angle and widens due to the destruction of the regular crystal structure of graphite and the decrease of its order. Fig. 4(b) shows the XRD pattern of the composites. The X-ray diffraction reflection at 2θ = 43.3°, 50.5° and 74.2° corresponds to the (111), (200) and (220) planes of Cu respectively, and the weak diffraction reflection at 2θ = 44.3°, 64.5° and 81.7° corresponds to the (110), (200) and (211) planes of Cr respectively.

Raman spectrum is a kind of scattering spectrum, which can be used to analyze the scattering spectrum with different frequency from the incident light to get the information of molecular vibration and rotation of carbon materials. Fig. 4(c) shows the Raman spectrum of GO. As shown in the figure, the D and G peaks of GO appear at 1351 cm^{-1} and 1581 cm^{-1} [57,58], respectively. The D peak at 1351 cm^{-1} involves a double resonance Raman process of defect scattering, so the defects of graphene will be reflected in its Raman D peak [59]. In addition, the G peak at 1581 cm^{-1} represents the in-plane stretching vibration of the C atom sp^2 hybrid. The peak intensity ratio of the D peak to the G peak can be used to characterize the defect size of GO. The I_D/I_G value of GO is 0.92, which indicates that the quality of GO is good and its original structure can be maintained after freeze-drying.

X-ray photoelectron spectroscopy (XPS) is a technique for analyzing the surface chemical properties of materials, which can be used to characterize the composition and chemical bonding state of GO. The elemental states and bonding mode of carbon atoms in the material can be obtained from the C 1s spectrum, as shown in Fig. 4(d–f). After fitting the C 1s spectrum, the characteristic signal peaks of GO were located at 284.70 eV, 286.50 eV, 287.10 eV and 288.40 eV, the characteristic signal peaks of 0.5GO-Cu/0.5$CeO_2$30Cr were located at 285.12 eV, 286.92 eV, 287.52 eV and 288.82 eV, the characteristic signal peaks of 1.0GO-Cu/0.5$CeO_2$30Cr were located at 285.23 eV, 287.03 eV, 287.63 eV and 288.93 eV, corresponding to the carbon double bond and single bond (C═C/C–C), epoxy group (C–O), carbonyl group (C═O) and carboxyl group (COOH) of sp^2 and sp^3, respectively [60–62]. In order to find the reduction of GO during SPS, the content percentages of different functional groups were calculated. Compared with GO, it can be seen from Table 1 that the proportions of C═C/C–C bonds in both composites increase, while the proportions of C═O and C–O bonds decrease. This shows that most of GO is reduced to RGO during SPS, which is a great significance to restore the conductivity of graphene. Fig. 4(g–i) show the O 1s spectra of GO and two composites. The characteristic peaks of oxygen atom appear in the O 1s spectrum of the composites, as shown in Fig. 4(g), in addition to the lattice oxygen of ceria at 532.23 eV, an obvious shoulder peak is observed at 530.58 eV, representing the oxygen absorbed in hydroxyl, carboxyl and epoxy groups, the same is true in Fig. 4(i).

3.3. Analysis of mechanical properties of composites

The comprehensive properties of relative density, conductivity, Vickers hardness and tensile strength of the two composites are shown in Table 2. Compared with the conductivity of Cu/0.5$CeO_2$30Cr without GO doping, the conductivity of the composite doped with 0.5 wt% GO reaches 64.59 %IACS, which is increased by 12.88%. In the sintering process, GO can be reduced into RGO with good conductivity. In addition, according to the XPS analysis, the content of GO decreased, and the effect of RGO on the conductivity of the composite was more significant than GO, so the conductivity of the composite doped with GO was improved. Although the functional groups of GO cannot completely remove during SPS sintering process, which will lead to a slight decrease in conductivity, the relative density of the composites was improved because the pressure reached 30 MPa during SPS sintering process. These factors are the reasons for the slight increase in conductivity of the composites doped with GO. In addition, the composites doped with 1.0 wt% GO have low conductivity due to the agglomeration of GO. The Vickers hardness of the two composites with GO was increased by 19.97% and 50.78% respectively. The dispersed nano-CeO_2 and Cr_3C_2 particles can RGO to strengthen the composites, inhibit dislocation movement and improve the hardness of the composites. Good electrical contact must have good mechanical properties and processing performance. Too low tensile strength will lead to mechanical wear performance degradation of electrical contact, and cannot meet the requirements of harsh service conditions. The tensile test results of the composite are shown in Fig. 5. Compared with Cu/0.5$CeO_2$30Cr composites, the tensile strength of the two kinds of GO composites increased 44.80% and 31.73% respectively. It means that the strengthening effect of adding 0.5 wt% GO is much better under the existing experimental conditions.

Table 1
Area percentages of different carbon bonds.

Sample	C=C/C–C	C–O	C=O	COOH
GO	36.65%	28.23%	26.96%	8.16%
0.5GO-Cu/0.5$CeO_2$30Cr	61.97%	16.15%	11.44%	10.44%
1.0GO-Cu/0.5$CeO_2$30Cr	49.70%	19.32%	17.74%	13.24%

Table 2
Comprehensive properties of composites.

Sample	Relative density/%	Electrical conductivity/% IACS	Vickers hardness/ HV	Tensile Strength/ MPa
Cu/ 0.5$CeO_2$30Cr	98.14	57.22	110.88	247.86
0.5GO-Cu/ 0.5$CeO_2$30Cr	99.05	64.59	133.02	358.91
1.0GO-Cu/ 0.5$CeO_2$30Cr	98.37	60.19	167.18	326.54

3.4. Microstructure analysis of composites

The SEM image and EDS diagram of the composites 0.5GO-Cu/0.5$CeO_2$30Cr、1.0GO-Cu/0.5$CeO_2$30Cr are shown in Fig. 6. It can be seen that the Cr particles are evenly distributed on the dispersed copper matrix without obviously agglomeration. In addition, the surface of the substrate is compact without voids.

Fig. 7 shows the TEM and HRTEM images of 0.5GO-Cu/0.5$CeO_2$30Cr

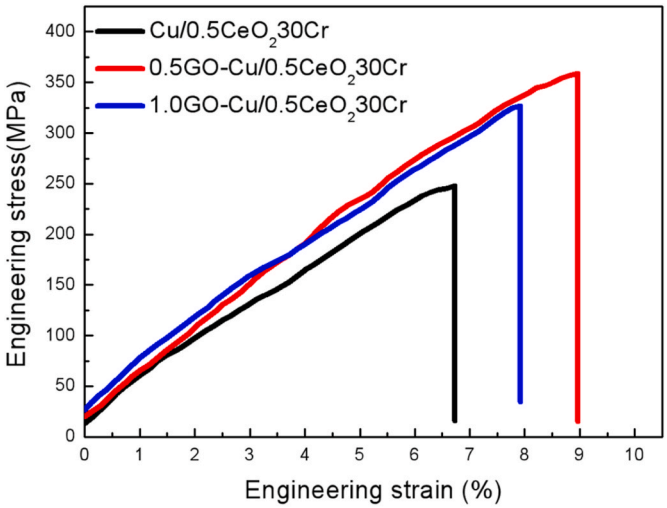

Fig. 5. Tensile stress-strain curves of different composites.

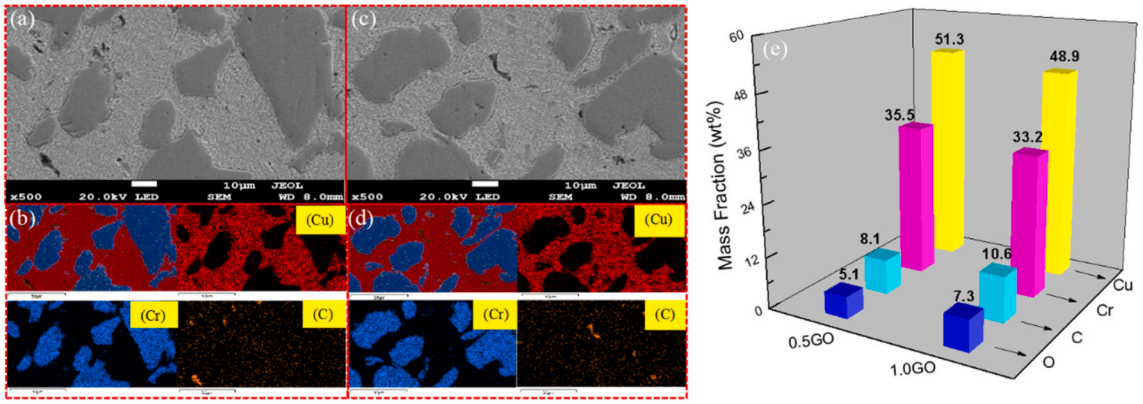

Fig. 6. SEM images and EDS analysis data of as sintered composites. (a, b) 0.5GO-Cu/0.5$CeO_2$30Cr; (c, d) 1.0GO-Cu/0.5$CeO_2$30Cr; (e) EDS data.

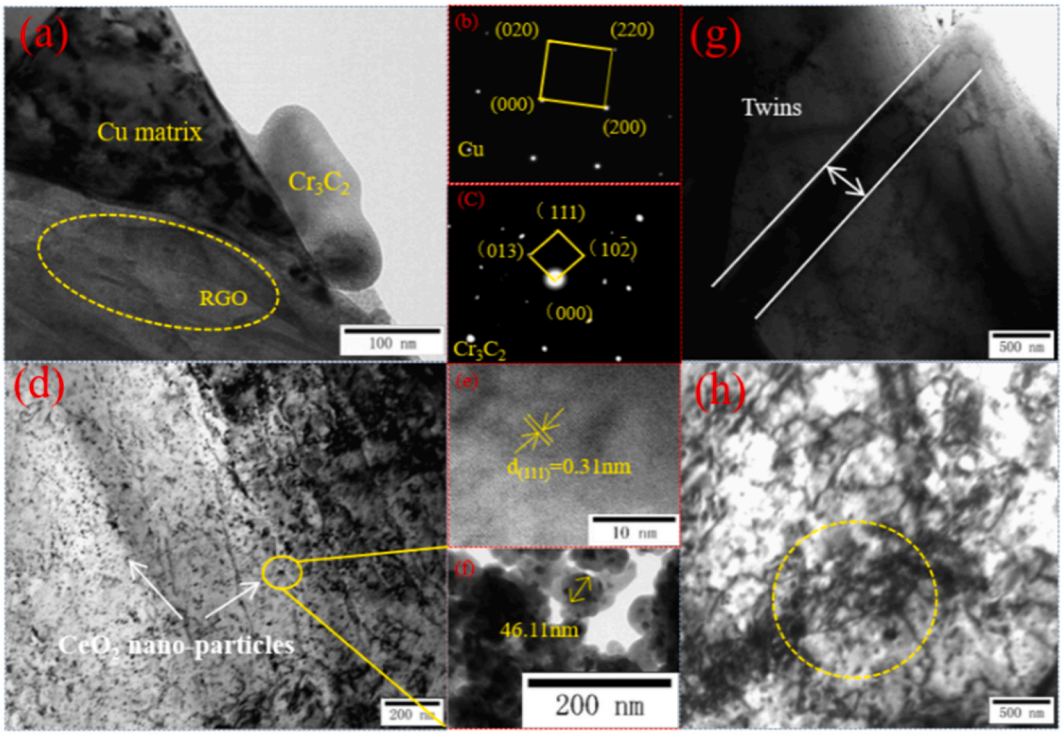

Fig. 7. TEM/HRTEM images of 0.5GO-Cu/0.5$CeO_2$30Cr composites. (a, d, e, f, g, h) high resolution microstructure; (b, c) selected area diffraction pattern.

composite. It can be seen from Fig. 7(a) that the copper matrix, RGO and carbon chromium compound Cr_3C_2 formed by carbon and chromium combine well after SPS. Fig. 7(b) shows the diffraction pattern of copper matrix. In Fig. 7(a) and (d), some particles adhere to the corrugated sheets of RGO. Electron diffraction pattern in Fig. 7(c) shows that the particles formed in situ between copper and RGO are Cr_3C_2. Cr_3C_2 has high hardness, good wettability to copper and strong oxidation resistance. Therefore, these Cr_3C_2 particles play an important role in enhancing the interface bonding, and significantly improve the mechanical properties. In Fig. 7(d), it can be seen that the dislocation is fixed by CeO_2 particles. They have a strong pinning effect, which hinders the movement of dislocations and improves the strength of copper matrix. Fig. 7(e) shows the TEM image of CeO_2 nanoparticles with clearer resolution, which effectively confirms the crystal structure of the material. From the figures, we can clearly observe a series of lattice planes with lattice spacing of 0.31 nm, which correspond to the (111) crystal plane of CeO_2 cubic fluorite structure. It can be seen from Fig. 7(f) that the particle size of ceria nanoparticles ranges from 40 to 50 nm. In addition, as shown in Fig. 7(g), some twins are formed in the copper matrix, which can hinder dislocation movement and grain boundary migration and play an important role in strengthening the material. Fig. 7(h) shows partial dislocation entanglement, and high dislocation density exists in some regions of the matrix, which improves the strength and hardness of the composite.

3.5. *Electrical contact properties of composites*

Fig. 8 shows the SEM images and three-dimensional profiles of two kinds of GO doped composite contacts after 5000 cycles under 25 V voltage and 30 A current. It can be seen from Fig. 8, some bumps and depressions are formed on the surface of anode and cathode.

Fig. 9 shows the erosion morphology of the electrical contact under high power electron microscope. In Fig. 9(a and b), the typical arc erosion characteristics such as splashing protrusions, pores, droplets, and cracks are formed on the contact surface. At high arc temperature, Cu first melts and splashes to form droplets or spreads and then solidifies

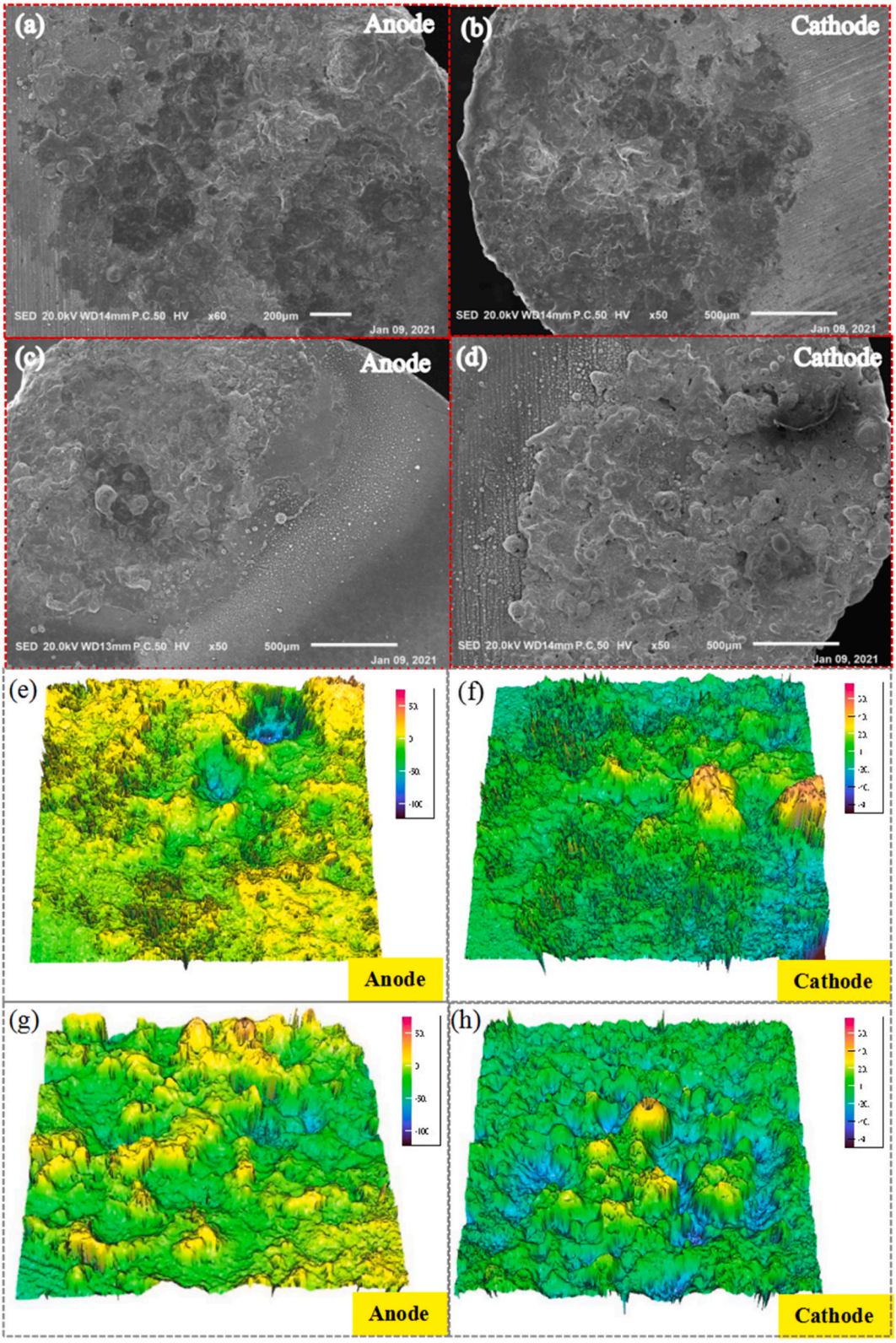

Fig. 8. SEM images and corresponding three-dimensional profile: (a, b, e, f) 0.5GO-Cu/0.5$CeO_2$30Cr; (c, d, g, h) 1.0GO-Cu/0.5$CeO_2$30Cr.

rapidly, resulting in a large amount of Cu erosion [63]. When the contact is disconnected, the porosity is that the surface temperature of the contact material drops rapidly, and the solubility of the metal to the gas also decreases, so that the gas breaks out from the metal and forms pores. Pores can reduce the mechanical strength of the contact surface, and even cause cracks. The cracks may extend in the matrix or cause the material surface to fall off. The cracks are the result of a variety of factors. Because the temperature of the metal surface decreases when it is disconnected, the liquid metal solidifies rapidly, resulting in the increase of dislocation density on the contact surface, the uneven distribution of stress in each area of the material, and the crack source will be formed.

Fig. 10(a–c) shows the change trend of mass and total mass of

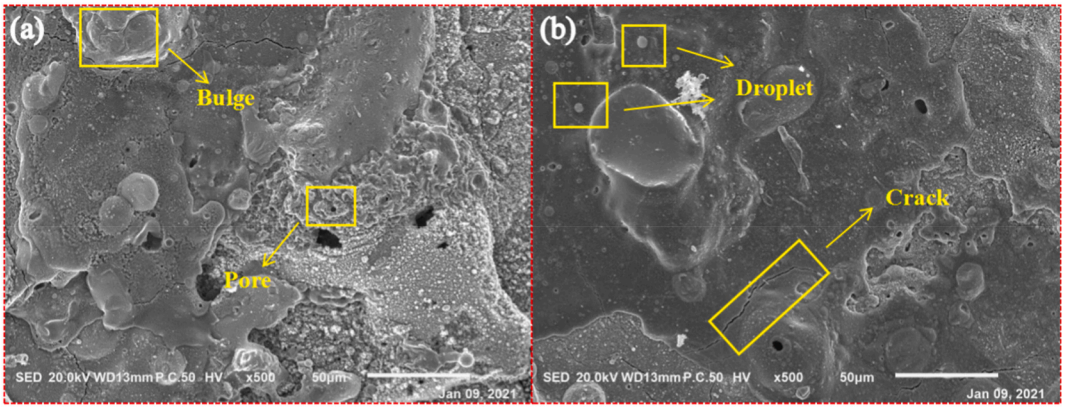

Fig. 9. High power arc erosion morphology of composite electrical contacts. (a) bulge, pore; (b) droplet, crack.

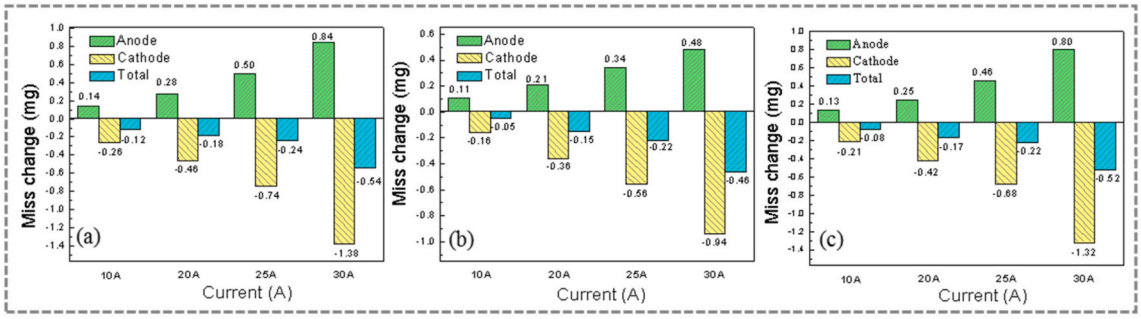

Fig. 10. Mass transfer of electrical contacts with different materials. (a) Cu/0.5CeO$_2$30Cr; (b) 0.5GO-Cu/0.5CeO$_2$30Cr; (c) 1.0GO-Cu/0.5CeO$_2$30Cr.

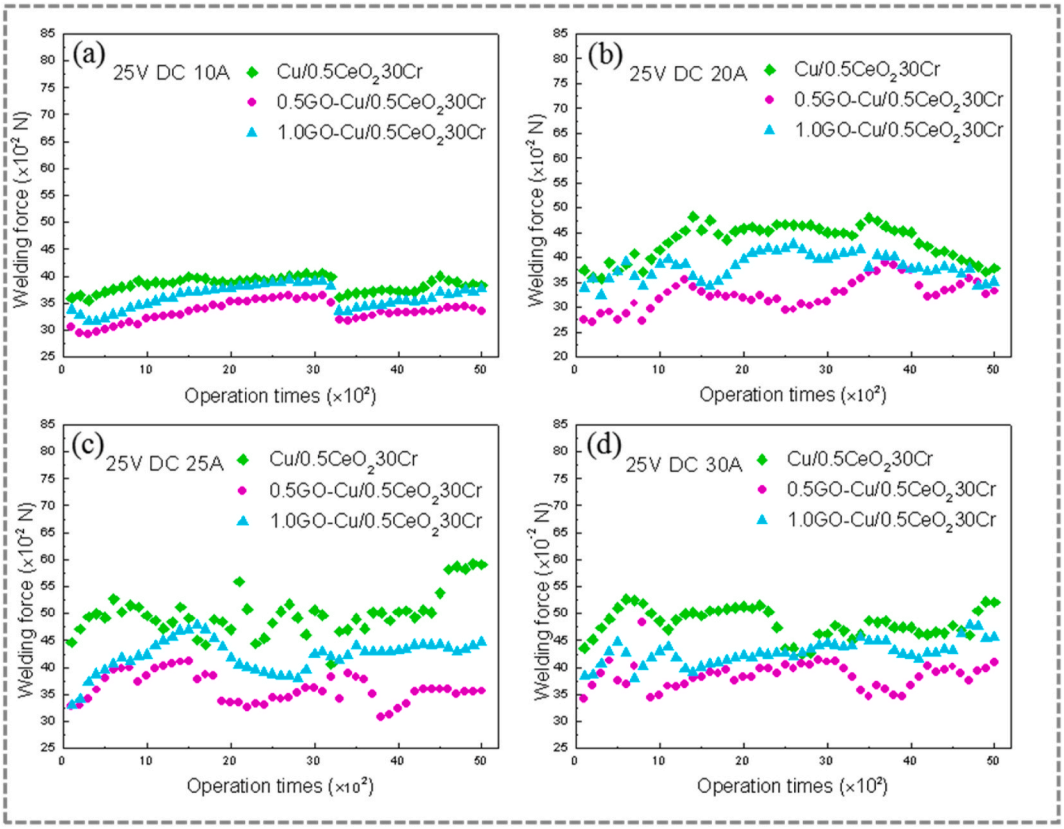

Fig. 11. Welding force of different composites at (a) 25 V DC, 10 A; (b) 25 V DC, 20 A; (c) 25 V DC, 25 A; (d) 25 V DC, 30 A.

cathode and anode contacts of Cu/0.5$CeO_2$30Cr, 0.5GO-Cu/0.5$CeO_2$30Cr and 1.0GO-Cu/0.5$CeO_2$30Cr after electrical contacts tests at DC 25 V and 10–30 A. It can be seen from the figures that the anode mass of the two composite contacts increases, the cathode mass decreases, and the total mass change is reduced, which means that a small part of the material is lost to the surrounding environment in the process of closing and breaking, and the material transfer increases gradually with the increase of the current from 10 A to 30 A. This is mainly because the current generated in the contact process of the electric contact is small, the arc column temperature is low, and the ionized charged particles are less. The main reason for maintaining the arc combustion is that the cations gather on the cathode surface which makes up for the insufficient electric field emission. And the cations gather at the cathode, and the continuous contraction of the arc increases the heat flux of the arc into the cathode, which causes the cathode material to transfer to the anode, and gradually increases with the increase of the current; the total mass change is negative, which means that a small amount of material is lost to the surrounding environment with the melting, evaporation and splashing during the arc erosion process. The mass transfer of 1.0GO-Cu/0.5$CeO_2$30Cr electrical contact samples under test conditions is greater than 0.5GO-Cu/0.5$CeO_2$30Cr electrical contact. The main reason is that the electrical conductivity of unreduced graphene oxide sheet and Cr_3C_2 and other new phases is not good under high temperature conditions, and the heat generated by the arc cannot be effectively dispersed, resulting in the deepening of contact erosion.

Fig. 11 shows the welding force variation curves of the three composites at DC 25 V and 10–30 A. The welding force variation ranges of Cu/0.5$CeO_2$30Cr, 0.5GO-Cu/0.5$CeO_2$30Cr and 1.0GO-Cu/0.5$CeO_2$30Cr are 0.24 N–0.52 N, 0.27 N–0.48 N and 0.28 N–0.47 N, respectively. It can be seen from the curves that the welding force of various contacts increases gradually with the increase of test current, and under each test condition, the welding force of Cu/0.5$CeO_2$30Cr is the largest, followed by 1.0GO-Cu/0.5$CeO_2$30Cr composite, and the welding force of 0.5GO-Cu/0.5$CeO_2$30Cr composite is the lowest, which means that the contact material has the best welding resistance. In addition, the tensile strength of 0.5GO-Cu/0.5$CeO_2$30Cr composite is higher than 1.0GO-Cu/0.5$CeO_2$30Cr composite, and its hardness is lower than 1.0GO-Cu/0.5$CeO_2$30Cr composite.

3.6. Discussion

Based on the above analysis, a possible carbide formation/evolution mechanism of GO-Cu/0.5$CeO_2$30Cr composite is proposed, as shown in Fig. 12. GO was prepared by oxidation of graphite with strong oxidants such as potassium permanganate and concentrated sulfuric acid. After mixing with copper powder, chromium powder and nano ceria, GO was sintered by SPS. During the sintering process, some functional groups of GO were reduced and transformed into RGO. Nano ceria particles attached to the surface of RGO, which plays the role of strong pinning effect can effectively hinder the movement of dislocations, enhance the interface bonding, and improve the mechanical properties of composites. During the sintering process, the surface of RGO will be slightly damaged and amorphous carbon will be formed. Once the amorphous carbon layer is formed, Cr atoms first diffuse to the amorphous carbon layer region. When the Cr concentration reaches the critical value, Cr atoms react with the active carbon atoms in the amorphous carbon layer to form Cr_3C_2. The growth process continues until all the active carbon atoms are exhausted. Because the growth of Cr_3C_2 is accompanied by the generation of new amorphous carbon, the new amorphous carbon formed between adjacent Cr_3C_2 layers/nanoparticles is transformed into new Cr_3C_2, which serves as a bridge to connect the Cr_3C_2 layers/nanoparticles. In this case, Cr_3C_2 may coalesce to form larger Cr_3C_2 nanoparticles. These Cr_3C_2 particles play an important role in enhancing the interface bonding and coupling between RGO and Cu, and significantly improve the mechanical properties.

In the process of using electrical contact, the change of material quality directly affects the quality and efficiency of electrical contact. When the current is small, the contact material emits electrons on the cathode surface, and the cations gather on the cathode surface to improve the electric field strength. The arc in the cathode area shrinks and the current density increases, which makes the area near the cathode ionize and makes up for the deficiency of electric field emission. The accumulation of the final cations causes the increase of the heat flux, and transfer of cathode material to anode. When the current increases, the temperature of the arc column increases and the number of charged particles needed to maintain the arc increases. It is no longer dependent on the emission of electrons from the cathode and the ionization of the cathode contraction region, and the phenomenon of arc contraction in the cathode region disappears. In order to maintain the arc and minimize its voltage, the arc column in the anode region shrinks, and the arc has instantaneous and concentrated heat input to the anode contact, so that the material is transferred from the cathode to the anode. The contact material melts under the action of arc heat, which makes it easy to observe the splash phenomenon in the test. Because when the arc discharges, the arc heat melts part of the contact material and produces a molten pool. In this way, the metal splashes out from the contact area in

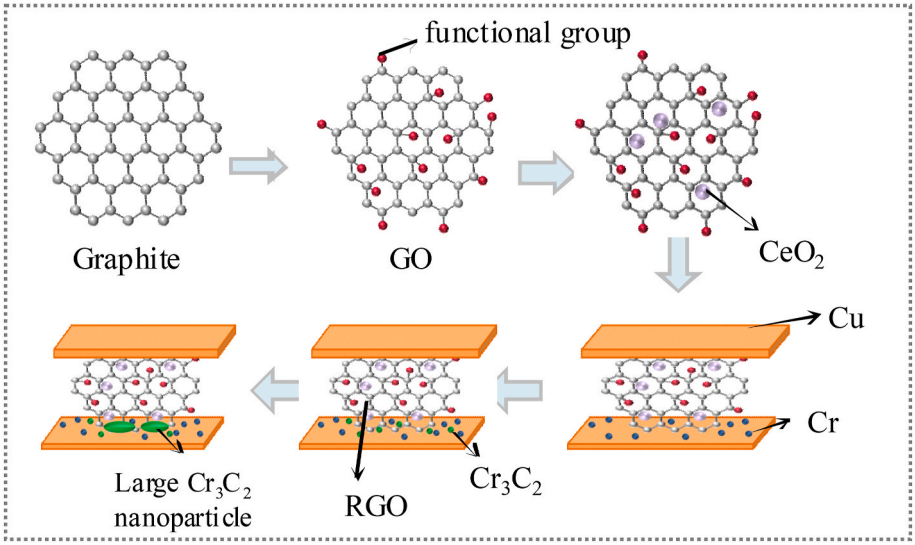

Fig. 12. Schematics of the possible carbide formation/evolution mechanism in composite.

the form of small droplets, resulting in melt splashing, leading to mass transfer and loss [64]. The total mass change of the two composites is negative, which indicates that there is environmental loss when the melt splashes out of the anode. In addition, at each current, the mass transfer of contact containing 1.0 wt% GO is the largest at each current, because the conductivity of the contact containing 1.0 wt% GO is lower.

4. Conclusion

(1) GO with good quality was prepared by improved Hummers method. Graphene oxide, cerium oxide nanoparticles, copper and chromium composite powders were obtained by freeze-drying, which ensured the complete structure and uniform dispersion of GO.
(2) GO-Cu/0.5$CeO_2$30Cr was prepared by spark plasma sintering and metal powder solidification during the sintering process, GO is reduced to RGO. Cr_3C_2 fixed dislocations formed in situ enhance the interface bonding and cause work hardening by coupling.
(3) The relative density of the two composites doped with GO is more than 98%, the Brinell hardness is increased by 19.97% and 50.78%, the tensile strength is increased by 44.80% and 31.73%.
(4) Some bumps and depressions are formed on the surface of anode and cathode respectively. The material transfer direction of the two composites is from cathode to anode. 0.5GO-Cu/0.5$CeO_2$30Cr composite has the best welding performance.

Declaration of competing interest

The authors declare that they have no known competing financial interests or personal relationships that could have appeared to influence the work reported in this paper.

Acknowledgments

This work was supported by the Outstanding Talents Innovation Fund of Henan Province (ZYQR201912164), Key Scientific Research Projects of Higher Education in Henan Province (21A430013), Natural Science Foundation of Henan Province (202300410144) and the National Natural Science Foundation of China (52071134).

References

[1] C. Salvo, R.V. Mangalaraja, R. Udayabashkar, M. Lopez, C. Aguilar, Enhanced mechanical and electrical properties of novel graphene reinforced copper matrix composites, J. Alloys Compd. 777 (2019) 309–316, https://doi.org/10.1016/j.jallcom.2018.10.357.
[2] X. Gao, H.Y. Yue, E. Guo, H. Zhang, X.Y. Lin, L.H. Yao, et al., Mechanical properties and thermal conductivity of graphene reinforced copper matrix composites, Powder Technol. 301 (2016) 601–607, https://doi.org/10.1016/j.powtec.2016.06.045.
[3] E. Hong, B. Kaplin, T. You, M. Suh, Y.S. Kim, H. Choe, Tribological properties of copper alloy-based composites reinforced with tungsten carbide particles, Wear 270 (9) (2011) 591–597, https://doi.org/10.1016/j.wear.2011.01.015.
[4] F. Shehata, A. Fathy, M. Abdelhameed, S.F. Moustafa, Preparation and properties of Al_2O_3 nanoparticle reinforced copper matrix composites by in situ processing, Mater. Des. 30 (7) (2009) 2756–2762, https://doi.org/10.1016/j.matdes.2008.10.005.
[5] X.H. Guo, K.X. Song, S.H. Liang, Y.J. Zhou, X. Wang, Relationship between the MgO_b/Cu interfacial bonding state and the arc erosion resistance of MgO/Cu composites, J. Mater. Res. 32 (19) (2017) 3753–3760, https://doi.org/10.1557/jmr.2017.321.
[6] V. Rajkovic, D. Bozic, M.T. Jovanovic, Properties of copper composites strengthened by nano- and micro-sized Al_2O_3 particles, Int. J. Mater. Res. 101 (3) (2013) 334–339, https://doi.org/10.3139/146.110278.
[7] J.J. Qi, X. Gao, N.T. Huang, Mechanical fault diagnosis of a high voltage circuit breaker based on high-efficiency time-domain feature extraction with entropy features, Entropy 22 (4) (2020) 478–493, https://doi.org/10.3390/e22040478.
[8] S. Wan, L. Chen, L.J. Dou, J.P. Zhou, Mechanical fault diagnosis of HVCBs based on multi-feature entropy fusion and hybrid classifier, Entropy 20 (11) (2018) 847–865, https://doi.org/10.3390/e20110847.
[9] X.H. Zhang, Y. Zhang, B.H. Tian, Y.L. Jia, M. Fu, Y. Liu, et al., GO effects on the Al_2O_3-Cu/35W5Cr composite properties, J. Mater. Sci. Technol. 37 (2) (2020) 185–199, https://doi.org/10.1016/j.jmst.2019.08.014.
[10] A.A. Razi-Kazemi, M. Abdollah, Novel high-frequency-based diagnostic approach for main contact assessment of high-voltage circuit breakers, IET Gener., Transm. Distrib. 12 (5) (2018) 1121–1126, https://doi.org/10.1049/iet-gtd.2017.0884.
[11] X.H. Zhang, Y. Zhang, B.H. Tian, Y.L. Jia, Y. Liu, K.X. Song, et al., Thermal deformation behavior of the Al2O3-Cu/(W, Cr) electrical contacts, Vacuum 164 (2019) 361–366, https://doi.org/10.1016/j.vacuum.2019.03.054.
[12] A. Papillon, S. Roure, H. Schellekens, J.M. Missiaen, J.M. Chaix, E. Rigal, Investigation on the chemical reactions affecting the sinterability and oxide content of Cu-Cr composites during the solid state sintering process, Mater. Des. 113 (2017) 353–360, https://doi.org/10.1016/j.matdes.2016.09.038.
[13] H.C. Fang, F.H. Luo, K.H. Chen, Effect of intermetallic phases and recrystallization on the corrosion and fracture behavior of an Al-Zn- Mg-Cu-Zr-Yb-Cr alloy, Mater. Sci. Eng., A 684 (2017) 480–490, https://doi.org/10.1016/j.msea.2016.12.009.
[14] C.J. Xu, S. Li, Y. Zhang, Y.J. Li, J. Zhou, G.W. Qin, Synthesis of CuO_x-CeO_2 catalyst with high-density interfaces for selective oxidation of CO in H_2-rich stream, Int. J. Hydrogen Energy 44 (8) (2018) 4156–4166, https://doi.org/10.1016/j.ijhydene.2018.12.152.
[15] D.Y. Chen, H.G. Zhu, S. Yang, N.J. Li, Q.F. Xu, H. Li, et al., Micro–nanocomposites in environmental management, Adv. Mater. 28 (47) (2016) 10443–10458, https://doi.org/10.1002/adma.201601486.
[16] M. Ramachandran, R. Subadevi, M. Sivakumar, Role of pH on synthesis and characterization of cerium oxide (CeO_2) nano particles, Vacuum 161 (2019) 220–224, https://doi.org/10.1016/j.vacuum.2018.12.002.
[17] S. Kumar, K. Kumari, F.A. Alharthi, F. Ahmed, R.N. Aljawfi, P.A. Alvi, Investigations of TM (Ni, Co) doping on structural, optical and magnetic properties of CeO_2 nanoparticles, Vacuum 181 (5) (2020) 109717, https://doi.org/10.1016/j.vacuum.2020.109717.
[18] S. Chahal, S. Singh, A. Kumar, P. Kumar, Oxygen-deficient lanthanum doped cerium oxide nanoparticles for potential applications in spintronics and photocatalysis, Vacuum 177 (4) (2020) 109395, https://doi.org/10.1016/j.vacuum.2020.109395.
[19] T.K. Mishra, A. Kumar, S.K. Sinha, B. Gupta, Wear behavior and XRD analysis of reinforced copper matrix composite reinforced with Cerium Oxide (CeO_2), Mater. Today 5 (14) (2018) 27786–27794, https://doi.org/10.1016/j.matpr.2018.10.014.
[20] P. Mayilsamy, S.P. Kumareshbabu, K. Nayan, S.A. Srinivasan, Mechanical property study on C90300 copper composites reinforced with rare earth oxide, Mater. Today 27 (2020) 2533–2536, https://doi.org/10.1016/j.matpr.2019.09.231.
[21] S.W. Lu, S. Wang, G.D. Wang, J.C. Ma, X.Q. Wang, H.L. Tang, Wearable graphene film strain sensors encapsulated with nylon fabric for human motion monitoring, Sensor Actuator., A Phys 295 (2019) 200–209, https://doi.org/10.1016/j.sna.2019.04.038.
[22] A.K. Geim, K.S. Novoselov, The rise of graphene, Nat. Mater. 6 (7131) (2007) 183–191, https://doi.org/10.1038/nmat1849.
[23] S. Stankovich, D.A. Dikin, G.H.B. Dommett, M.K. Kohlhaas, E.J. Zimney, E. A. Stachet, et al., Graphene-based composite materials, Nature 442 (7100) (2006) 282–286, https://doi.org/10.1038/nature04969.
[24] C. Lee, X.D. Wei, J.W. Kysar, J. Hone, Measurement of the elastic properties and intrinsic strength of monolayer graphene, Science 321 (5887) (2008) 385–388, https://doi.org/10.1126/science.1157996.
[25] S.C. Tjong, Recent progress in the development and properties of novel metal matrix nanocomposites reinforced with carbon nanotubes and graphene nanosheets, Mater. Sci. Eng. R 74 (10) (2013) 281–350, https://doi.org/10.1016/j.mser.2013.08.001.
[26] N.V. Ponraj, A. Azhagurajan, S.C. Vettivel, et al., Graphene nanosheet as reinforcement agent in copper matrix composite by using powder metallurgy method, Surf. Interfaces 6 (2017) 190–196, https://doi.org/10.1016/j.surfin.2017.01.010.
[27] I.W. Frank, D.M. Tanenbaum, dZAM. Van, P.L. Mceuen, Mechanical properties of suspended graphene sheets, J. Vac. Sci. Technol., B 25 (6) (2007) 2558–2561, https://doi.org/10.1116/1.2789446.
[28] L.J. Fu, L. Zhang, J.K. Xiao, K.C. Zhou, Sliding wear behavior of copper-based composites reinforced with graphene nanosheets and graphite, Trans. Nonferrous Met. Soc. China 25 (2015) 3354–3362, https://doi.org/10.1016/S1003-6326(15)63970-X.
[29] C.L.P. Pavithra, B.V. Sarada, K.V. Rajulapati, T.N. Rao, G. Sundararajan, A new electrochemical approach for the synthesis of copper-graphene nanocomposite foils with high hardness, Sci. Rep. 4 (4049) (2014) 4049–4055, https://doi.org/10.1038/srep04049.
[30] L.D. Wang, Z.Y. Yang, Y. Cui, WeiB, S.C. Xu, J. Sheng, et al., Graphene-copper composite with micro-layered grains and ultrahigh strength, Sci. Rep. 7 (2017) 41896–41905, https://doi.org/10.1038/srep41896.
[31] K. Chu, F. Wang, Y.B. Li, X.H. Wang, D.J. Huang, H. Zhang, Interface structure and strengthening behavior of graphene CuCr composites, Carbon 133 (2018) 127–139, https://doi.org/10.1016/j.carbon.2018.03.018.
[32] K. Chu, C.C. Jia, Enhanced strength in bulk graphene-copper composites, Phys. Status Solidi 211 (1) (2014) 184–190, https://doi.org/10.1002/pssa.201330051.
[33] Y. Chen, X. Zhang, E. Liu, C. He, C.S. Shi, J.J. Li, et al., Fabrication of in-situ grown graphene reinforced Cu matrix composites, Sci. Rep. 6 (2016) 19363–19371, https://doi.org/10.1038/srep19363.
[34] X. Zhang, Y.X. Xu, M.C. Wang, E.Z. Liu, ZhaoNQ, C.S. Shi, A powder-metallurgy-based strategy toward three-dimensional graphene-like network for reinforcing copper matrix composites, Nat. Commun. 11 (1) (2020) 2775–2787, https://doi.org/10.1038/s41467-020-16490-4.
[35] H.W. Niu, H. Bian, D. Liu, J.H. Liu, X.G. Song, Z. Sun, et al., Microstructural evolution of Ti-6Al-4V/UD-C_f/LAS composites joint brazed by graphene

nanosheets reinforced composite filler, Vacuum 161 (2019) 176–185, https://doi.org/10.1016/j.vacuum.2018.12.027.
[36] Y.S. Su, Z. Li, Y. Yu, L. Zhao, Z.Q. Li, Q. Guo, et al., Composite structural modeling and tensile mechanical behavior of graphene reinforced metal matrix composites, Sci. China Mater. 61 (1) (2018) 112–124, https://doi.org/10.1007/s40843-017-9142-2.
[37] A.K. Kasar, G.P. Xiong, P.L. Menezes, Graphene-reinforced metal and polymer matrix composites, JOM (J. Occup. Med.) 70 (6) (2018) 829–836, https://doi.org/10.1007/s11837-018-2823-2.
[38] F. Nazeer, Z. Ma, L.H. Gao, A. Malik, M.A. Khan, S. Abrar, et al., Effect of graphene on thermal and mechanical properties of copper-titanium carbide composites, Vacuum 173 (4) (2019) 109100, https://doi.org/10.1016/j.vacuum.2019.109100.
[39] F. Nazeer, Z. Ma, L.H. Gao, S. Abrar, A. Malik, M.A. Khan, et al., Higher mechanical and thermal properties of Cu-rGO composites, Vacuum 180 (5) (2020) 109584, https://doi.org/10.1016/j.vacuum.2020.109584.
[40] C.Y. Wang, Y.S. Su, Q. Ouyang, D. Zhang, Enhanced mechanical behavior and fabrication of graphite flakes covered by aligned graphene nanoplatelets reinforced 2A12 aluminum composites, Vacuum 188 (9) (2021) 110150, https://doi.org/10.1016/j.vacuum.2021.110150.
[41] G.N. Mekgwe, O.J. Akinribide, S.O. Akinwamide, P.A. Olubambi, Fabrication of graphite reinforced TiCxNy by spark plasma sintering technique: a comparative assessment of microstructural integrity and nanoindentation properties, Vacuum 187 (5) (2021) 110144, https://doi.org/10.1016/j.vacuum.2021.110144.
[42] T. Yang, W.G. Chen, F.L. Yan, H.B. Lv, Y.Q. Fu, Effect of reduced graphene oxides decorated by Ag and Ce on mechanical properties and electrical conductivity of copper matrix composites, Vacuum 183 (4) (2020) 109861, https://doi.org/10.1016/j.vacuum.2020.109861.
[43] J.L. Ye, X.H. Chen, J.B. Li, C.Q. Liu, B. Wu, F.S. Pan, Microstructure and compressive properties of Mg-9Al composite reinforced with Ni-coated graphene nanosheets, Vacuum 181 (4) (2020) 109629, https://doi.org/10.1016/j.vacuum.2020.109629.
[44] S.L. Liang, S. Liu, Y. Zhang, M. Zhou, B.H. Tian, Y.F. G, Effect of in situ graphene-doped nano-CeO_2 on microstructure and electrical contact properties of Cu30Cr10W contacts, Nanotechnol. Rev. 10 (1) (2021) 385–400, https://doi.org/10.1515/NTREV-2021-0031.
[45] J.P. Kelly, O.A. Graeve, Spark plasma sintering as an approach to manufacture bulk materials: feasibility and cost savings, JOM (J. Occup. Med.) 67 (1) (2015) 29–33, https://doi.org/10.1007/s11837-014-1202-x.
[46] A. Nieto, D. Lahiri, A. Agarwal, Synthesis and properties of bulk graphene nanoplatelets consolidated by spark plasma sintering, Carbon 50 (2012) 4068–4077, https://doi.org/10.1016/j.carbon.2012.04.054.
[47] Z.A. Munir, U.A. Tamburini, The effect of electric field and pressure on the synthesis and consolidation of materials: a review of the spark plasma sintering method, J. Mater. Sci. 41 (2016) 763–777, https://doi.org/10.1007/s10853-006-6555-2.
[48] A.V. Ragulya, Consolidation of ceramic nanopowders, Adv. Appl. Ceram. 107 (3) (2008) 118–134, https://doi.org/10.1179/174367608X318844.
[49] G. Greczynski, L. Hultman, X-ray photoelectron spectroscopy: towards reliable binding energy referencing, Prog. Mater. Sci. 107 (2019) 100591, https://doi.org/10.1016/j.pmatsci.2019.100591.
[50] G. Greczynski, L. Hultman, The same chemical state of carbon gives rise to two peaks in X-ray photoelectron spectroscopy, Sci. Rep. 11 (1) (2021) 11195, https://doi.org/10.1038/S41598-021-90780-9.
[51] G. Greczynski, L. Hultman, Compromising science by ignorant instrument calibration-need to revisit half a century of published XPS data, Angew. Chem. 132 (13) (2020) 5002–5006, https://doi.org/10.1002/ange.201916000.
[52] G. Greczynski, L. Hultman, Reliable determination of chemical state in x-ray photoelectron spectroscopy based on sample-work-function referencing to adventitious carbon: resolving the myth of apparent constant binding energy of the C 1s peak, Appl. Sci. 451 (2018) 99–103, https://doi.org/10.1016/j.apsusc.2018.04.226.
[53] C.Q. Hua, S.H. Zhou, C.W. Zhou, W.D. Dou, H.N. Li, Y.H. Lu, et al., Work function modulation of graphene with binary mixture of Cu and C60F36, Carbon 179 (2021) 172–179, https://doi.org/10.1016/j.carbon.2021.04.022.
[54] P. Jaesung, L.W. Hyoung, H. Sung, S.S. Hyun, K.S. Bin, C. Kilwon, et al., Work-function engineering of graphene electrodes by self-assembled monolayers for high-performance organic field-effect transistors, J. Phys. Chem. Lett. 2 (8) (2011) 841–845, https://doi.org/10.1021/jz200265w.
[55] U. Saha, R. Jaiswal, T.H. Goswami, A facile bulk production of processable partially reduced graphene oxide as perior supercapacitor electrode materia, Electrochim. Acta 196 (1) (2016) 386–404, https://doi.org/10.1016/j.electacta.2016.02.203.
[56] P. Cui, J. Lee, E. Hwang, H. Lee, One-pot reduction of graphene oxide at subzero temperatures, Chem. Commun. 47 (45) (2011) 12370–12372, https://doi.org/10.1039/c1cc15569e.
[57] A.C. Ferrari, J.C. Meyer, V. Scardaci, C. Casiraghi, M. Lazzeri, F. Mauri, et al., Raman spectrum of graphene and graphene layers, Phys. Rev. Lett. 97 (18) (2006) 187401–187404, https://doi.org/10.1103/PhysRevLett.97.187401.
[58] P. Miranzo, C. Ramirez, B.R. Manso, L. Garzon, H.R. Gutiérrezc, M. Terrones, et al., In situ processing of electrically conducting graphene/SiC nanocomposites, J. Eur. Ceram. Soc. 33 (2013) 1665–1674, https://doi.org/10.1016/j.jeurceramsoc.2013.01.021.
[59] A. Das, B. Chakraborty, A.K. Sood, Raman spectroscopy of graphene on different substrates and influence of defects, Bull. Mater. Sci. 31 (2008) 579–584, https://doi.org/10.1007/s12034-008-0090-5.
[60] Q. Zhang, C. Cai, J.W. Qin, B.Q. Wei, Tunable self-discharge process of carbon nanotube based supercapacitors, Nano Energy 4 (2014) 14–22, https://doi.org/10.1016/j.nanoen.2013.12.005.
[61] D.X. Yang, A. Velamakanni, G. Bozoklu, S.J. Parka, M. Stollera, R.D. Piner, Chemical analysis of graphene oxide films after heat and chemical treatments by X-ray photoelectron and micro-Raman spectroscopy, Carbon 47 (2009) 145–152, https://doi.org/10.1016/j.carbon.2008.09.045.
[62] Y.X. Tang, X.M. Yang, R.R. Wang, M.X. Li, Enhancement of the mechanical properties of graphene-copper composites with graphene-nickel hybrids, Mater. Sci. Eng., A 559 (2014) 247–254, https://doi.org/10.1016/j.msea.2014.01.061.
[63] L.L. Dong, W.G. Chen, N. Deng, J.L. Song, J.J. Wang, Investigation on arc erosion behaviors and mechanism of W70Cu30 electrical contact materials adding graphene, J. Alloys Compd. 696 (2017) 923–930, https://doi.org/10.1016/j.jallcom.2016.12.044.
[64] Y. Hu, G.X. Chen, G.Q. Gao, et al., Study on material transfer in the process of contact strips rubbing against a contact wire with electric current, P. I. Mech. Eng. J. Eng. 230 (2) (2016) 202–211, https://doi.org/10.1177/1350650115595055.